Effect of Stress Level on the Microstructural Evolution of Clay under Creep

Dan Zhao, Mahdia Hattab, Pierre-Yves Hicher, Zhen-Yu Yin

Effect of Stress Level on the Microstructural Evolution of Clay under Creep

Dan ZHAO[1], Mahdia HATTAB[2], Pierre-Yves HICHER[3], Zhen-Yu YIN[4,5]

Abstract: Creep in clay can significantly affect long-term deformation evolution and therefore impact the safety of geotechnical structures. To improve our understanding of the mechanism of creep, we have examined the microstructural evolution of a kaolin clay sample submitted to creep under three-dimensional or axisymmetric loading conditions, focusing on the effect of the stress level. This experimental study identifies the local mechanisms in normally and over consolidated remolded clay samples during creep under triaxial conditions at different stress levels. The results show that the macro and micro behaviors of the kaolin clay are predominantly governed by the contractancy/dilatancy mechanism activated along stress paths at constant p'. Within the contractancy domain, the SEM observations showed that the microstructural anisotropy increased with the augmentation of the stress level. The microstructural evolution during creep can be attributed to changing patterns in particle reorientation and pore geometry, resulting in plastic strain hardening/softening as well as in viscous fluid flow. The evolution of the clay microstructure therefore depends on both the stress level and the OCR. The differences in the orientation pattern under creep appeared to be enhanced according to the contractancy/dilatancy mechanism. The dilative specimens exhibited particle orientations which were relatively random. The flattening/expansion of the micropores under creep corresponded to the contraction/dilation mechanism at the specimen scale. An attempt based on the analysis of the SEM photographs was made to evaluate the evolution of anisotropy during the different loading phases.

Key words: clay, creep, stress level, triaxial test, microstructure, SEM images, anisotropy

[1]Lecturer, College of civil engineering and architecture, Zhejiang University of Water Resources and Electric Power, Hangzhou, China

[2] Professor, Laboratoire d'Etude des Microstructures et de Mécanique des Matériaux, Université de Lorraine, CNRS UMR 7239, Arts et Métiers ParisTech, F-57000 Metz, France

[3] Professor Emeritus, Institut de Recherche en Génie Civil et Mécanique, CNRS UMR 6183, Ecole Centrale de Nantes, Université de Nantes, France.

[4] Associate Professor, Department of Civil and Environmental Engineering, The Hong Kong Polytechnic University, Hung Hom, Kowloon, Hong Kong, China.
[5]Corresponding author, Tel: (+852) 3400 8470, Fax: (+852) 2334 6389, Email: zhenyu.yin@polyu.edu.hk

Introduction

When a soil sample is under a state of constant effective stress, it deforms over time, which corresponds to the phenomenon of creep. Clayey soils usually display significant creep deformation in the form of prolonged settlements of foundations, tilts of geotechnical structures, or slippage of slopes and embankments, for instance (i.e. Mesri & Choi, 1985; Tavenas & Leroueil, 1981; O'Reilly et al., 1991; Rowe & Hinchberger, 1998; Mitchell & Soga, 2005; Karstunen & Yin, 2010; Yin et al., 2015, 2017; Zhu et al. 2014). Generally, the mechanical behavior of clay is determined by the microstructural state of the material and its evolution. (Hattab et al. 2010; Hattab & Favre, 2010; Hammad et al., 2013; Hattab et al., 2015; Xie et al., 2018; Gao et al., 2020; Yu et al. 2019). With regard to the creep behavior, experimental results generally show the development of strains in relation to microstructural changes, this phenomenon depending mainly on the loading history (Mitchell & Soga, 2005; Zhao et al., 2020).

On the scale of the specimen, the creep behavior of clay has been widely investigated through triaxial testing (Singh & Mitchell 1968; Bishop & Lovenbury HT, 1969; Mesri & Godlewski 1977; Tavenas et al. 1978; Tian et al., 1994; Zhao et al., 2019). In most of these studies, the effect of stress on the creep behavior of clay was described by time-dependent strain rates, where the axial strain (ε_1) and axial strain rate increased with the stress level. However, the development under creep of the volumetric strain (ε_v) appeared to be more complicated. The tests on undisturbed normally consolidated clayey soils under conventional triaxial creep, where the confining pressure σ'_3 was maintained constant, showed that the volumetric strain ε_v varied in positive correlation with the stress level as, for example, in the case of marine sediments (Tian et al., 1994). On the other hand, Kong et al. (2011) showed that under higher confining pressure, the volumetric creep strains of undisturbed Zhanjiang clay were quite close to each other at various stress levels. The influence of the stress level on the evolution of the volumetric strain during creep depended on the stress path in the study of Tavenas et al. (1978). By plotting the results in the p'-q plane, they found that an increased p' stress path caused an increase of the magnitude of the volumetric strain depending on the stress level; very small volume change was detected under different stress levels along constant p' stress path; an obvious dilatancy occurred continuously and up to failure under high stress level along a decreased p' stress path.

To better understand the influence of the loading history on creep behavior, Zhao et al. (2019) performed triaxial creep tests on saturated remolded clay along constant p' stress paths.

The results showed that the position of the stress level within the different volumetric domains (defined in the p'-q plane) controls in a significant way the evolution of the volumetric creep strain. The different volumetric strain domains were defined by Hattab & Hicher (2004) through purely deviatoric triaxial tests in which a pseudo-elastic zone corresponding to the pseudo-elastic volumetric domain proposed by Biarez & Hicher (1994) was determined. In this domain, the volumetric strain depended only on the variation of p', no volume change was observed during creep (Zhao et al., 2019).Beyond the pseudo-elastic domain, the volumetric strain evolution depended on the components of stress, the deviatoric stress q and the mean effective stress p'. Hence, the volumetric strain ε_v increased with the stress level under creep. These results suggest that the effect of stress, *i.e.* the stress level, on the macroscopic creep behavior still requires a clearer understanding.

At the microstructure scale, the observations usually showed an evolution of the microstructure during creep. Akagi (1994) concluded that creep was the result of the delayed deformation of micropores within the clay particles induced by the viscous flow of the micropore fluid. Sun (2007) stated that the creep of silty clay contains two aspects: particle rearrangement and expulsion of pore fluid from microfabric elements, *i.e.* the closure of the matrix micropores, the generation of microcracks and the expansion of macrocracks as the stress increases. In soft soils, Li et al. (2010) showed a pore variation related to creep, where a gradual change in the micropore properties revealed a micro-mechanism evolution of the clay structure. Xie et al. (2018) investigated the microstructure of a loess-like soil through triaxial creep tests. They stated that the creep was mainly related to the reorientation of particles and pores. They also revealed that the evolution of the meso-pores was the most important factor leading to the creep of these materials. The experimental results recently performed by Zhao et al. (2020) on Kaolin samples showed that the microstructural evolution during creep stages clearly depended on the stress history. Generally, the microstructure variations under creep followed the structural pattern developed under monotonic loading. Their study highlighted a creep dilatancy phenomenon strongly related to the expansion of micro pores and micro cracks within the overconsolidated clay specimens. Nevertheless, the evolution of the clay microstructure under different stress conditions during creep is still under discussion.

This study focuses on two specific aspects of creep development after purely deviatoric stress paths: *i*. the effect of the stress level along a given constant p' stress path; *ii*. the effect of the stress level at a constant stress ratio. Significant insight comes from analyzing the microstructure evolution along the different loading stages. The experimental approach

consists of performing a series of triaxial creep tests and identifying the microstructure, particle orientations, and pore properties along the creep stage. The latter analyses were quantified using the scanning electron microscopy (SEM) technique on different samples after triaxial loading. The local mechanisms explaining the development of the creep process in relation to the stress state were revealed by linking the microstructural characteristics to the mechanical behavior.

Material and experimental techniques

Material and triaxial test method

The soil selected for this research is an industrial Kaolin K13 clay whose liquid limit is 42%, plastic limit is 21% and specific gravity is 2.63. The compression index is 0.288 and the swelling index is 0.085. According to the measured grain size distribution, the mean dimensions of the clay "grains" fall into the range of 2.5 μm to 20 μm, which may concern both unit particles as well as aggregates of larger sizes. For the mechanical tests, cylindrical specimens, 75 mm in height and 50 mm in diameter, were cut from a one-dimensional pre-consolidated core.

The triaxial tests were carried out on saturated remolded kaolin specimens by using the GDS triaxial testing system. The tests included two categories: the triaxial shear group and the triaxial creep group. These two groups of tests were conducted following the same saturation, consolidation and shearing steps. Along with the triaxial shearing procedure, constant p' triaxial stress paths were applied up to a given stress level. The second group consisted in a series of creep tests performed at the same stress level. Both p' and q were kept constant for at least 7 days to measure the creep deformation. After the triaxial loading, all specimens were unloaded by steps. After having been retrieved from the cell, the specimens were enveloped in film paper, tin foil and paraffin, and then kept at constant temperature before being prepared for SEM analysis. Let us note that one can find the procedure of the sample preparation and the mechanical test principle described in more details in Zhao et al. (2019). The specification of the triaxial tests is summarized in Table 1. The specimen denomination corresponds to the loading condition. For example, for P_{010}-OCR4-q200, P_{010} represents the consolidation stress p'_{0i} = 1000 kPa; OCR4 represents an overconsolidation ratio equal to 4; the NC symbol represents normally consolidated specimens; q200 indicates that a deviatoric stress of 200 kPa was applied during constant p' triaxial shearing. The subscript "shear/creep" represents the

two categories of tests.

The loading state at the end of the shear/creep for these two groups of triaxial tests is shown in the (p'-q) plane in Fig. 1. In this plane, the contractancy, no-volume change (pseudo-elastic), and dilatancy domains identified by Hattab & Hicher (2004) were superimposed (Zhao et al., 2019). In this study, we performed tests under stress conditions marked by numbered lines in Fig. 1. Line ① represents two tests having the same OCR under different stress levels (named *SL)* and belonging to the contractancy domain; line ② represents two tests under different *SL*s with the same OCR, one within the contractancy domain and the other within the no-volume change domain. The two series of tests aimed to analyze the role of the stress level; line ③ corresponds to the three tests located along a constant stress ratio (named η, where $\eta = 0.67$) line, but with different OCRs, thus different history of loading of the samples, their loading paths evolving within the contractancy or dilatancy domain.

Microscopic identification techniques

Specimen preparation

The preparation of an undisturbed small sample for microstructure observation plays a key role in this microscopic study. After triaxial testing, the core zone of each cylindrical specimen was cut into a soil board to a dimension of 30 mm × 30 mm × 10 mm. Thereafter, a sub-specimen of 10 mm in height was extracted from the soil board. The surface layer of the sub-specimen was notched slightly in the middle section in order to obtain an undisturbed observation plane. Note that the length direction of the sub-specimen was referenced as perpendicular to the axial stress (σ'_1) applied to the cylindrical specimen in the triaxial cell. Specific preparation permitting to preserve the clay fabric of the sub-specimens were carried out before introducing them inside the SEM cell (Delage & Pellerin, 1984; Hattab et al. 2010; Hammad et al. 2013; Gao et al. 2020; Zhao et al. 2020). With the following stages of sub-specimen preparation, a dry and clean section for identifying the microstructure of the kaolin clay by SEM could be obtained: *i.* dehydration through the freeze-drying method; *ii.* fracturing stage to obtain a fresh section for the observation; *iii.* metallization of the section with gold. It should be noted that in previous studies, the SEM images with magnifications of 1000× to 5000× were suitable for the identification of the clay microstructure (Hattab et al., 2010; Zhang & Cui, 2017; Gao et al., 2020 and Zhao et al., 2020). Thus, 3000× magnified images were selected for this research. For a representative result to be obtained, a large number of images is required for a statistical interpretation. Around 20 typical areas were

156 randomly selected on each observed surface for each specimen.

157 ***Image processing methods***

158 Kaolinite particles are shaped as rigid platelets that can form parallel-stacked mineral layers
159 (Fig. 2a). From the view of the vertical plane, the kaolin particles that contain the orientation
160 information exist as ellipsoid flakes. Thus, the particles can be simulated one by one through
161 short lines that have the same length and the same orientation as the major axis length and
162 orientation of the ellipsoid flakes (Fig. 2b). Let us note that the axisymmetric loading
163 condition of the specimens implies that the particles seen by face, which are parallel to the
164 image, correspond to the particles of the surface seen by their edge. Thus, they are not
165 simulated. The orientations of the represented lines with respect to the X-axis can be
166 measured by the angle θ (0˚~180˚), where θ equal to 0˚/180˚ means that the particle is
167 perpendicular to σ'_1, see the illustrations in Fig. 2c. The imaging plane was divided into 12
168 quadrants, each of which equals to 15˚. The number and the percentage of particles oriented
169 towards each quadrant were calculated, represented by the orientation curve in Fig. 2c. The D
170 line in Fig. 2c, with a mean percentage of 8.3%, represents a perfectly isotropic
171 microstructure (Hattab & Fleureau, 2011).

172 In Fig.2a, the raw micrograph obtained by SEM is represented by the greyscale image.
173 Generally, the SEM image presents the pore spaces in a darker greyscale compared to the
174 solid particles. Thus, the pore space and the solid particle can be discriminated. In this study,
175 the pore properties (orientation and dimension) were partly identified by the Image J software.
176 The original image was transformed into the binary image (Fig. 2d) by setting an optimal
177 threshold value. Then, the connected pores were separated through the distance transform and
178 watershed segmentation algorithm. Afterwards, using an internal Image J feature, the
179 segmented pores were fitted with ellipses, keeping as much as possible identical areas, aspect
180 ratios, orientations and centroids (Fig. 2e). The detailed identification method refers to the
181 works of Hicher et al. (2000), Hattab & Fleureau (2010), Gao et al. (2020) and Zhao et al.
182 (2020).

183 After the identification of particles and pores, different local parameters were deduced: the
184 orientation index I_{or} (Eq. 1) which expresses the anisotropy of the structure (Hicher et al.,
185 2000) and the pore roundness R_s (Eq.2) which characterizes the shape of a pore.

186 $$I_{or} = \frac{k + l + m}{r + s + t} \quad (1)$$

$$R_s = \frac{B}{A} \quad (2)$$

Where I_{or} varies from 0 (for a totally anisotropic arrangement) to 1 (for an ideal isotropic structure); s is the maximum percentage (the peak value in Fig. 2c); r and t are the percentages of the two zones beside the maximum one; k, l, m are the percentages of the zones perpendicular to the zones r, s and t, respectively. R_s varies from 0 (for a very elongated pore) to 1 (for an equiaxed pore); A and B are the major and minor axis length of the fitted ellipse, respectively.

Strain mechanisms under creep and microstructure features

The strain mechanisms of kaolin specimens under a pure deviatoric stress path have been widely discussed by Hattab & Hicher (2004) and then by Zhao et al. (2019, 2020). The latter framework is taken in this study to discuss the influence of the stress level on creep after purely deviatoric paths, as well as the influence of the stress history by keeping constant the stress ratio. Let us consider the representative groups of NC tests and the tests with OCR=1.5 represented by line ①and line ② (Fig. 1), respectively. For line ②, the two stress levels are located in two different volumetric domains: the pseudo-elastic domain for the lower stress level (q=200 kPa), and the contraction domain for the higher stress level (q=445 kPa).

In what follows, the analyses are focused on both the macroscopic behavior and the obtained microstructure features.

Tests on normally consolidated samples

For normally consolidated (NC) samples under loading paths within the contractancy domain, a contractant behavior, as expected, was detected from the beginning of the monotonic loading (Fig. 3) and the compression was more pronounced under a higher stress level. The experimental results show a good consistency within the same loading interval, which permits to directly identify the mechanisms of evolution related to the stress level. During creep, a contractive behavior was also obtained (Fig. 4a) and the contractive creep deformation was larger under a higher stress level. The evolution of the volumetric creep strain ($\varepsilon_{v\text{-}creep}$) under a purely deviatoric stress path for NC samples is consistent with the results under constant σ'_3 by Tian et al (1994), and those under an increasing p' stress path by Tavenas et al. (1978) and by Sekiguchi (1973). Fig. 4b shows that a higher stress level

produced a relatively larger volumetric strain rate, but the difference tended to become negligible after about 1000 minutes in the creep phase.

Fig. 5 presents representative SEM photos of the test P_{010}-NC-q670 within the contractancy domain after shear and after creep. One can see that the particles were mostly arranged face-face along oriented planes and reoriented by groups towards a given orientation after creep (Fig. 5b) in a more pronounced way than after the monotonic shear loading (Fig. 5a). The preferential microfabric of clay along purely deviatoric stress path is quite different from the random orientation pattern identified after isotropic consolidation, see for instance Hicher et al. (2000), Hattab &Fleureau (2011) and Gao et al. (2020). This highly oriented microstructure combined with its densification appears to be directly related to the contractive behavior at the specimen scale.

Slightly overconsolidated case - OCR=1.5 samples

Mechanical behavior analysis

The stress-strain relations for OCR=1.5 samples under monotonic loading are shown in Fig. 6. The P_{010}-OCR1.5-$q445_{shear}$ test showed a clear and very marked contractancy starting at q = 227 kPa, which was very close to the limit of the pseudo-elastic domain. The path evolved afterward within the contractancy domain, reaching a volumetric strain of ε_v= 0.58% at the stress level of q = 445 kPa. For the four shear tests, no significant volumetric strains were observed, given the accuracy of the experimental system, when the paths evolved within the pseudo-elastic domain.

The evolutions of the volumetric creep strains as a function of time are presented in Fig. 7a. For specimens located within the pseudo-elastic domain (P_{010}-OCR1.5-$q200_{creep}$), the result showed that a volumetric strain evolution alternated between very small contractancy and very small dilatancy. These results seem to be directly related to the constant stress control condition, thus it is reasonable to assume that no volumetric strain under creep developed within this pseudo-elastic domain (Zhao et al., 2019). For soil creeping within the contractancy domain, P_{010}-OCR1.5-$q445_{creep}$, the contractancy was more pronounced and developed continuously. A linear tendency of the volumetric creep strain rate was observed after about 1000 minutes (Fig. 7b), corresponding to the well-known primary creep. Fig. 7b shows that, in the early period of creep, the relationship between $log\dot{\varepsilon}_{v-creep}$ and $logt_{creep}$ is curved for the three specimens within the contractancy domain. Afterward, the volumetric strain rates varied inside a quite narrow band after t_{creep}=1000 minutes. Let us note that Tian et

al. (1994) obtained similar tendencies on normally consolidated marine sediments from the Gulf of Mexico and Zhu (2007) on Hong Kong marine sediments.

Microstructure features

Fig. 8 shows the representative SEM photos for the samples sheared under different stress levels, whereas Fig. 9 shows the representative images after creep under different stress levels.

In Fig. 8 the vast majority of isolate particles is plate-shaped and form aggregates with a maximum diameter of about 10 μm. The mean size of an individual particle is about 1.5 μm in length. Generally, the particles are face-face associated, as shown by thin layers in the side view of the SEM photos. In Fig. 8a, one can see that the groups of particles are partly arranged edge-face and partly face-face. These results are similar to what was obtained for specimens with OCR=2.5 located within the pseudo-elastic domain (Zhao et al., 2020), which suggests that similar microstructures are related to this particular domain. With the increase of the stress level within the contractancy domain, a clear contractancy developed at the sample scale resulted in an obvious preferential oriented pattern at the microscopic scale (Fig. 8b). The particles were mostly face-face along certain preferential oriented planes, showing an anisotropy which was also observed by Hattab & Fleureau, (2011). Globally the system here shows a trend towards a denser structure. Thus, rearrangements in the clay microstructure developed with the increase of the stress level along purely deviatoric monotonic loading.

In the case of the P_{010}-OCR1.5-$q200_{creep}$ specimen within the pseudo-elastic domain, the microfabric tended to evolve isotropically rather than anisotropically after a certain creeping time (Fig. 9a), similarly to the state of the structure for the specimen after shear (Fig. 8a). As for the P_{010}-OCR1.5-$q445_{creep}$ specimen under a higher stress level within the contractancy domain, the microstructure rearranged towards an apparent anisotropy. Obviously, these results highlight two different features depending on the stress level, as well as on the domain where the creep occurred.

Creep phenomenon - Microstructural study

Following the experimental procedure described in *Section 2.2.2*, the evolution of the particle orientation and the pore properties related to different loading histories will be examined in this section.

Influence of stress level under the same OCR

Clay particle orientation mechanism for NC samples

Fig. 10 presents the global particle orientation curves of 4 normally consolidated samples under different stress levels located within the contractancy domain, following the condition of line ① (Fig. 1).The global orientation of the clay particles is illustrated in the form of orientation curves. The oriented curves of specimens at q=200 kPa and 670 kPa after shear were drawn from 10 photos representing 4347 particles and 14 photos representing 7156 particles, respectively (Fig. 10a). The curves for the two specimens after creep were obtained from 14 photos representing 7227 particles and 19 photos representing 7170 particles, respectively, as shown in Fig. 10d.

Fig. 10a shows that the orientation curves for the two sheared samples within the contractancy domain depart from the structural isotropic D line, as identified on the same clay after an isotropic loading by Gao et al. (2020). The peak values for the percentage of particle orientation of the two specimens fall into the range of 150° to 165°, which means that the majority of individualized particles and particle groups are oriented in this direction (as illustrated on the representative image in Fig. 5a). This result observed at the local level demonstrates the existence of an anisotropic microfabric, which corresponds to the contractancy at the macroscopic level of the specimen. Furthermore, with larger compression of the specimen under a higher stress level, more obvious structural anisotropy can be seen, the orientation curve being further apart from the D line (Fig. 10a).

In Fig. 10b and Fig. 10c, the microstructure analyses show that the orientation curves exhibit more marked peaks after creep than after shear. For the two samples after creep, the orientation angles are quite similar to those obtained after shear tests, but with higher magnitudes (Fig. 10d). These results suggest that particle rearrangement continues during creep, with more particles joining the preferential direction, as shown in Fig. 5b. The peak value **P** in Fig. 10 indicates that the principal orientation is located between 150° to 165° under two stress levels. This can be attributed to the induced anisotropy developed during creep. It is interesting to note in Fig. 10d that the particle orientation for samples after creep seems to be independent of the stress level. This phenomenon may highlight a dominating contractancy mechanism related to creep within the volumetric contractancy domain.

At the microscopic scale, the NC specimens show the development of the anisotropy combined with densification at the macro scale, the majority of the particles being oriented in a preferential direction. These results are in agreement with those previously obtained under

monotonic loading for instance by Hicher et al. (2000), Hattab et al. (2010) and more recently Gao et al. (2020). During creep, the anisotropy continues to evolve, resulting in the increase of the number of particles oriented in a preferential direction (see the example of test P_{010}-NC-q670 in Fig. 5).

Clay particle orientation mechanism for OCR=1.5 samples

A qualitative analysis of the photos taken at different observation points for the lightly overconsolidated specimens is shown in Fig. 11. The oriented curves at q=200kPa and 445kPa after shear were drawn from 11 photos (5639 particles) and 14 photos (7156 particles), respectively (Fig. 11a). By comparing the two curves, it appears that the curve at q = 200 kPa has moved closer to the perfect isotropic D line, whereas at q = 445 kPa, the curve has departed away from the D line with an obvious peak value in the 150° to 165° direction (point **P** in Fig. 11a), which means that the majority of the individualized particles are oriented in this direction (see the representative image in Fig. 8b). The global orientation curves of the clay particles clearly show the influence of the stress level during the monotonic loading. For a clay specimen under a lower stress level located within the pseudo-elastic domain, the preferential reorientation of the clay particles is not dominant; it seems that the initial isotropic microstructure developed during isotropic consolidation has not been completely erased. Under higher stress level within the contractancy domain, an anisotropic orientation tends to develop along the purely deviatoric loading phase, resulting in a large number of clay particles rotating towards a preferential direction.

Fig. 11b and 11c present the particle orientation before and after creep under different stress levels. It can be seen in Fig.11b that, for the two samples loaded within the pseudo-elastic domain, a slight change in particle orientation was identified after creep. The limited particle orientation evolution during creep would not introduce an obvious macroscopic deformation. The results for the test P_{010}-OCR1.5-q445 are abnormal compared to the continuous contractancy at the sample scale (Fig. 7a). Less structural anisotropy was identified after creep than after shear. This abnormal experimental result may be due to the observation spots on SEM images of the specimen P_{010}-OCR1.5-$q445_{shear}$; this aspect will require further experimental verification. It should be noted that the results of P_{010}-OCR1.5-$q445_{shear}$ give at least a reasonable structural anisotropy. Thus, the results of this test were maintained without any strong conclusion being drawn from them.

Fig.11d compares the global particle orientation of the lightly overconsolidated specimens after creep under two different stress levels. The shapes of the orientation curves appear quite

consistent with those after shear (Fig.11a). This may demonstrate that the particle rearrangement during creep follows the same structure pattern as the one formed in the monotonic loading stage. For the sample at q = 200kPa creeping within the pseudo-elastic domain, very limited structure rearrangement took place during creep. The microstructure evolution is in agreement with the findings obtained at the macroscopic scale, showing that no volumetric strain took place along the p' constant stress path. For the sample at q = 445 kPa creeping within the contractancy domain, the dominated direction (around 160°) obtained for the sample after shearing (Fig.11a) was maintained.

Pore property evolution for NC samples

The particle orientation modes have to be associated with the pore space and its geometric distribution including orientation, roundness and elongation. The coupling of both systems can define the state of the material at the representative elementary volume scale.

The particles rearranged during loading, which resulted in a certain preferred orientation; consequently, the corresponding inter-particle pore geometry can provide complementary information on the structural rearrangement. Generally, the global pore orientation is consistent with the particle orientation identified in *Section 4.1.1*, as shown in Gao et al. (2020) and Zhao et al. (2020). For these tests following the same p' constant stress path, the distribution pattern of pores depends on the magnitude of the stress applied to the specimen.

For the two normally consolidated samples sheared within the contractancy domain, the global pore orientations under different stress conditions (Fig. 12a) are quite consistent, as expected, with the particle orientations (Fig. 10a). After the monotonic loading, the structural anisotropy increased under a higher stress level (Fig. 12a), resulting in a curve clearly further from the isotropic D_{pore} line. The D_{pore} line in terms of pore orientation has a similar meaning as the depolarization line (D line) of particle orientation. However, a slightly weaker anisotropy of the micro pores for the specimen after creep under higher stress level could be observed (Fig. 12b), which may indicate that a specific mechanism controlled the pore evolution under creep.

As illustrated in Fig.2, the pores identified in SEM images can be fitted by ellipses. The shape characteristic of the pores can thus be evaluated through the roundness of the fitted ellipse by Eq.2. Figs. 13-14 compare the global particle shapes of four normally consolidated specimens under different stress levels. All the roundness curves show unimodal distributions

with a marked peak of a dominant roundness relatively distant from *Rs* =1 (Figs. 13a & 14a), which indicates that most pore shapes are clearly elongated.

After the monotonic loading, the mean lengths of the pores increased with the stress level (Fig. 13b), with L_{mean}= 0.566 μm under q = 200 kPa and L_{mean}= 0.713 μm under q = 445 kPa; whereas the mean diameters showed an opposite trend, with D_{mean}= 0.284 μm under q = 200 kPa and D_{mean}= 0.142 μm under q = 445 kPa (Fig. 13c). These results indicate that the pores were elongated as well as flattened with the increase of the specimen contraction developed under a higher stress level. During the creep phase, taking the example of test P_{010}-NC-q200, the pores tend to be flatter after the creep stage, illustrated by a smaller mean pore diameter in the specimen after creep (Fig. 14c) than in the specimen after shearing (Fig. 13c), whereas the pore length before and after creep remained relatively unchanged (Fig. 13b &14b). In the case of the specimen under a higher stress level, the mean pore length was shortened after creep. Furthermore, the mean pore parameters for the two creep specimens appear quite similar (Fig. 14) regardless of the difference in the stress level. The same consistency can be seen in the particle orientation in Fig. 10d, which highlights a dominating contractancy mechanism related to creep in this volumetric domain.

Pore property evolution for OCR=1.5 samples

In the case of lightly overconsolidated samples, the structural anisotropy increased under a higher stress level (Fig. 15a), resulting in a curve clearly further from the isotropic D_{pore} line. After a certain duration in the creep phase, the differences in the orientation of pores under different stress levels decreased (Fig. 15b).The structural isotropy evolved for the specimen under q = 445kPa, whereas a structural anisotropy developed for the sample under q = 200 kPa, resulting in a final orientation close to the horizontal.

The statistical results presented in Fig. 16 bring more insight. The pore shape variations of four lightly overconsolidated specimens after shear and after creep are shown. Compared to the curves drawn from the four NC samples, the differences in the pore shapes with OCR = 1.5 are more significant. In Fig. 16a, it can be seen that the mean roundness for the 2 specimens under q = 445kPa (*Rs* = 0.45) is smaller than for the 2 specimens under q = 200kPa (*Rs* = 0.55). This means that the pores tend to be generally smaller under higher stress levels, as shown by a clearly lower percentage of the mean length and mean diameter in Fig. 16b and 16c. The variation of the pore shape with *SL* is reflected especially in the change of the mean diameter (Fig. 16c). It can be seen that the difference in pore diameter between the two specimens sheared under two different stress levels is mainly in the range of D>0.28 μm,

409 which indicates that the largest pores are more likely to contract with the increase of the stress
410 level, resulting in a denser structure.

411 For the two P_{010}-OCR1.5-q200 specimens within the pseudo-elastic domain, no volume
412 change occurred at the macroscopic level under the creep phase (see Fig. 7a). The mean pore
413 shape is the same for the sheared and the creep specimens for which Rs_{mean} is 0.55, L_{mean} and
414 D_{mean} is 0.713 μm and 0.357 μm, respectively. The phenomenon appears similar to what was
415 observed for an OCR=2.5 specimen also located within the pseudo-elastic domain (Zhao et al.,
416 2020).

417 For the two P_{010}-OCR1.5-q445 specimens within the contractancy domain, the change of
418 the pore shape during the creep phase concerns mainly the pore diameter, with a higher
419 percentage of pores for D＞0.284μm and a smaller percentage of pores for D＜0.284μm in
420 the creep specimen than in the sheared specimen (Fig. 16c). This result may indicate that the
421 contraction under creep occurs mainly by the flattening of the smaller pores.

422 **Microstructures under same stress ratio but different loading histories**

423 For specimens under a stress level located on the line ③ (Fig. 1), corresponding to a stress
424 ratio η = 0.67, the results show a contractancy for both the NC and the OCR=1.5 specimens,
425 whereas for the highly overconsolidated clay a dilatancy was detected at the first stage of the
426 monotonic loading. During the creep phase, contractancy or dilatancy developed continuously
427 as can be observed in Fig. 17a, the volumetric creep strain rate (the absolute value of $\dot{\varepsilon}_{v-creep}$
428 was introduced for the case of OCR=4) decreasing with the increase of OCR in the early stage
429 of the creep test, and then tending to be similar at the later stage of the creep test (Fig. 17b).

430 ***Clay particle orientation mechanism***

431 The particle orientation curves for the three specimens are shown after shearing in Fig.
432 18a and after creep in Fig. 18b. The shapes of the orientation curves for the two stress levels
433 located within the contractancy domain are quite consistent, showing both a clear structural
434 anisotropy development. For the highly overconsolidated specimen $(P_{010}\text{-OCR4-q200})_{shear}$,
435 located within the dilatancy domain, the orientation curve moves towards the D line, meaning
436 that the microstructure tends towards a structural isotropy. The isotopic microstructure
437 appears here related to the dilatant behavior at the macroscopic scale.

438 For the three specimens after creep (Fig. 18b), the differences are increased, due to the
439 particle rearrangement under the creep phase with different stress paths. The percentage of

particles in the privileged direction (150° to 165°) decreased with OCR, meaning that the induced anisotropy or isotropy tended to increase.

Pore property evolution – Orientation, roundness and elongation

As expected, the evolution of the pore orientation appears to be consistent with the particle orientation. A significant influence of the OCR on the pore orientation, linked to the dilatancy mechanism, could be observed. As shown in Fig. 19a, the dilative specimen P_{010}-OCR4-$q200_{shear}$ had smaller maximum percentages, which indicates that more random micropore orientations developed within the specimen during loading. The contractancy or the dilatancy continued to develop during the creep phase, resulting in the orientation curves to approach the D_{pore} line with the increase of OCR as can be observed in Fig. 19b.

The statistical results in Fig. 20 show the distribution of the pore shapes for the three specimens under different OCRs after the creep phase, the stress levels being located along the constant stress ratio line η = 0.67. Altogether, as shown previously in Fig. 16, the creep stage led to an extension of the tendencies activated by the shear loading stage. For the 2 specimens creeping within the contractancy domain (NC and OCR=1.5 samples), the pore shape tended to show very similar roundness distribution curves (Fig. 20a). However, for the highly overconsolidated specimen with OCR = 4 located within the dilatancy domain, the curve shifted to the right, highlighting globally rounder pores. The influence of the stress path on the evolution of the pore shape under creep pertains mainly to the evolution of the pore diameter: a clear increase in the mean pore diameter when OCR increased from 1 to 4 could be observed in Fig. 20c. The opening/expansion of the micro pores associated with a depolarization orientation contributes here to the dilatancy mechanism at the sample scale.

Discussions

Based on the current statistical results of particles and pores properties, the evolution of the clay microstructure is clearly dependent on the stress history, as well as on the stress level in the triaxial loading stage. In the creep stage, the development of contractancy/dilatancy at the sample scale is accompanied by a continuous rearrangement of the soil structure. In what follows, the microstructural evolution related to the creep mechanism will be discussed in relation to the stress level influence. The illustrations of the conceptual models within different volumetric strain domains under different stress conditions are shown in Fig.22, where the black dotted lines represent the orientation of groups of particles and the blue circles represent the state of the pores.

Within the contractancy domain for normally consolidated samples, the depolarization (or the isotropic microstructure) first induced by the isotropic triaxial loading was progressively erased along the purely deviatoric stress path (see the sketches within the contractancy domain after shear in Fig.22). The influence of the deviatoric stress seems predominant in the particle rotation mechanism towards privileged orientations. When the stress level increase leads to larger strains, the rotation of the particles becomes more apparent and their orientation progressively tends towards privileged orientation lines of 150° to 165°. The rearrangement of the soil structure under stress accompanied by the free water flowing out of the soil element induces the decrease of D_{mean} along with the increase of L_{mean} (Fig. 21b and Fig.22). Consequently, the contacts between particles gradually increase from a random edge-face contact after isotropic consolidation to a face-face contact along monotonic loading. The specimen experiences a denser structure with the increase of *SL* in this domain governed by the contractancy mechanism. In the creep phase, plastic strains developed at the macro scale. At the microscopic scale, the deformation of the pores either in length or in diameter (Fig. 21b and Fig.22) and, as a consequence, the drainage of the pore fluid, led to an increase of the induced anisotropy, *i.e.*, the decrease of the orientation index I_{or} (Fig. 21a).

For the lightly overconsolidated samples loaded from the pseudo-elastic domain up to the contractancy domain, two different orientation modes could be characterized (see the sketches within the pseudo-elastic domain after shear in Fig.22). At the end of the monotonic loading, the particles of the specimen remaining within the pseudo-elastic domain are mainly associated by groups oriented along oblique planes. The development of this structural mode is assumed to be related to the very light contractancy phenomenon in monotonic loading under low stress levels, where the isotropy is still dominant. During creep, a null volumetric change is assumed at the macroscopic scale. At the microscopic scale, the particle orientation and especially the porosity do not evolve significantly in the creep phase (Fig. 22b).The quite limited macroscopic deformation alternating between contractancy and dilatancy was found to be provoked by the slight fluctuation in the GDS system trying to maintain a constant stress condition (Zhao et al., 2019). The microfabric under the fluctuating stress/strain corresponds to a progressive adjustment of the clay structure to reach equilibrium under the external effective stresses.

However, when the stress level reaches the contractancy domain, the contractancy mechanism is activated; the clay particles are mainly associated face-to-face and oriented in an oblique direction mode (Fig. 22). Although a continuous contractancy of the lightly

overconsolidated sample can be observed, the microstructure evolution under creep is, in this case, less pronounced than in the NC samples. A decrease of anisotropy for the specimen after creep was obtained (Fig. 23a); however, the porosity evolution remained quite limited (Fig. 23b). It may be assumed that a weakened or delayed mechanism exists due to the loading history within the pseudo-elastic domain, which requires deeper analyses.

The experimental tests conducted in this study aimed at contributing to a better understanding of the micro-macro mechanisms in clay related to creep. According to the analysis of the microstructure through SEM images, the creep mechanism can be seen as the displacement of groups of clay particles, called aggregates. The relative sliding occurs mainly between adjacent groups of particles. A promising approach to the micro-macro constitutive modelling is to treat clay as an assembly of aggregates interacting by means of contact (normal and shear) forces and to attempt to derive stress-strain relationships on this basis. The contact forces, together with the contact orientation of the particles, constitute the fabric of a clay sample.

The orientation distribution of the particle deposition angles was obtained through SEM images. For a contact between two particles, the contact orientation is defined as the normalized vector connecting the centroids of two particles, as shown in Fig. 24 in the local coordinates, where θ and β are the angles of inter-particle contact, *n*, *s*, and *t* represent the components of the local forces in the three directions of the local coordinate system. For a particulate assembly, the contact orientation distribution can be characterized by an angular distribution $E(\theta)$, which is given by:

$$E(\theta) = \frac{1}{4\pi}[1 + a\cos 2(\theta - \theta_a)] \quad (3)$$

where a defines the magnitude of anisotropy and θ_a defines the direction of anisotropy (Rothenburg & Bathurst, 1989; Wang & Yin, 2020). The parameter a can be fitted from the contact orientation distribution using Eq.(3). When a = 0 the distribution is perfectly isotropic. The values of the fabric parameter a obtained after shear and creep are summarized in Fig. 25. For the isotropically loaded sample, a value of a close to zero was obtained. For samples located within the contractancy/dilatancy volumetric domain, the magnitude of anisotropy a increased/decreased along the creep phase, resulting in a higher/lower a value for the samples under creep than that for the samples under shear. Meanwhile, the changes of θ_a in these two zones indicate that the direction of anisotropy also evolved during creep. It should be noted that for samples located within the pseudo-elastic volumetric domain (P_{010}-OCR1.5-q200), the

direction of anisotropy θ_a remained almost unchanged after shear and after creep, while the magnitude of anisotropy a increased to some extent. The calculated parameters in Eq.(3) match well the experimental observations.

Based on SEM photos from different loading stages corresponding to different stress states and plastic strains, the fabric evolution can be characterized as a function of stresses and plastic strains. The equation of a and θ_a can then be applied to micromechanical/multiscale models, such as the recently developed micromechanics-based elastoplastic model for granular materials, clays and soil mixtures by authors (Chang & Hicher 2005,Yin et al. 2009; Yin et al. 2014; Zhao et al. 2018), since these kind of models use the orientation distribution function of contacts to consider the soil anisotropy. Our ultimate objective is to formulate the fabric tensor as a function of the macroscopic strain/stress tensor relating to creep. The development of such model is in progress and will be the topic of a future paper.

Conclusion

This study attempted to characterize the microstructure of remolded kaolin subjected to various triaxial stress paths followed by a creep stage. Ten triaxial tests were performed on both normally and overconsolidated samples under different stress levels and stress ratios. Afterward, the SEM technique was used to identify the microstructural features of the clay before and after creep. From these analyses, the following points can be observed:

- The evolution under creep depends on the deformation at the end of the monotonic loading. The microstructure pattern of particles and pores identified through SEM images showed results that are consistent with the tendencies at the sample scale.
- The influence of the stress level on the creep deformation in normally consolidated samples followed the same pattern as what was obtained along monotonic loading paths. For normally consolidated specimens within the contractancy domain, the particles and pores showed preferential orientation, indicating the development of a structural anisotropy and this tendency continued during creep. The increase of the stress level led to a decrease of the pore diameter after creep, resulting, from plastic strain hardening as well as viscous flow, in a more stable structure.
- The influence of the stress level on the creep deformation of lightly overconsolidated clay depended on the position of the stress state within a given volumetric domain. Structural anisotropy and decrease of pore diameter were also obtained for a lightly

overconsolidated specimen within the contractancy domain under a high stress level. However, for a lightly overconsolidated specimen under a lower stress level within the pseudo-elastic domain, the clay structure was in an intermediate state, the microstructural evolution during creep in this domain being quite limited.

- The changes in loading history and variations in both stress level and OCR provoked different behaviors. The dilative specimens exhibited relatively random orientation. The differences in the orientation pattern appeared enhanced in agreement with the contractancy/dilatancy mechanism during creep. The flattening/expansion of micropores under creep corresponded to the contraction/dilation mechanism at the specimen scale within the different volumetric domains.

Data availability statement

All data that support the findings of this study are available from the corresponding author upon reasonable request.

Acknowledgement

The financial supports provided by the China Scholarship Council for the first author, the GRF project (Grant No. 15217220) and NSFC/RGC Joint Research Scheme (Grant No. N_PolyU534/20) from the Research Grants Council (RGC) of Hong Kong, the National Natural Science Foundation of China (grant numbers 51808407 and 51608281) are gratefully acknowledged.

References

Akagi, H. 1994. "A physico-chemical approach to the consolidation mechanism of soft clays." *Soils Found.*, 34(4), 43–50. https://doi.org/10.3208/sandf1972.34.4_43.

Biarez, J., and Hicher, P.-Y. 1994. "Elementary mechanics of soil behaviour: saturated remoulded soils." A.A. Balkema, Rotterdam.

Bishop, A. W., and Lovenbury, H. T. 1969. "Creep characteristics of two undisturbed clays." *Proc. 7th Int. Conf. Soil Mech. Found. Eng.*, Mexico City, 1:29–37.

Chang, C.S. and Hicher, P.-Y. 2005 "An elastoplastic Model for Granular Materials with Microstructural Consideration." *Int. J. of Solids and Structures*, Vol. 42, 14: 4258-4277.

Delage, P., and Pellerin, F. M. 1984. "Influence de la lyophilisation sur la structure d'une argile sensible du Québec." [Influence of freeze-drying on the structure of a sensitive clay from Quebec].[In French] *Clay Min.*, 19(2), 151–160. https://doi.org/10.1180/claymin.1984.019.2.03.

602 Gao, Q. F., Hattab, M., Jrad, M., Fleureau, J.-M., and Hicher, P.-Y. 2020. "Microstructural
603 organization of remoulded clays in relation with dilatancy/contractancy phenomena."
604 *Acta Geotech.*, 15, 223–243. https://doi.org/10.1007/s11440-019-00876-w.

605 Hammad, T., Fleureau, J.-M., and Hattab, M. 2013. "Kaolin/montmorillonite mixtures
606 behaviour on oedometric path and microstructural variations." *Euro. J. Environ. Civil*
607 *Eng.*, 17(9), 826–840. .

608 Hattab, M., Bouziri-Adrouche, S., and Fleureau, J.-M. 2010. "Évolution de la microtexture
609 d'une matrice kaolinitique sur chemin triaxial axisymétrique." [Evolution of the
610 microtexture of a kaolinitic matrix on axisymmetric triaxial path]. [In French] *Can.*
611 *Geotech. J.*, 47(1), 34–48. https://doi.org/10.1139/T09-098.

612 Hattab, M., and Favre, J. L. 2010. "Analysis of the experimental compressibility of deep
613 water marine sediments from the Gulf of Guinea." *Marine and Petroleum Geology*, 27
614 (2), 486–499. https://doi.org/10.1016/j.marpetgeo.2009.11.004.

615 Hattab, M., and Fleureau, J.-M. 2010. "Experimental study of kaolin particle orientation
616 mechanism." *Géotechnique*, 60(5), 323–331.
617 https://doi.org/10.1680/geot.2010.60.5.323

618 Hattab, M., and Fleureau, J.-M. 2011. "Experimental analysis of kaolinite particle orientation
619 during triaxial path." *Int. J. Numer. Anal. Methods Geomech.*, 35 (8), 947–
620 968.https://doi.org/10.1002/nag.936

621 Hattab, M., and Hicher, P.-Y. 2004. "Dilating behavior of overconsolidated clay." *Soils*
622 *Found.*, 44(4), 27–40. https://doi.org/10.3208/sandf.44.4_27.

623 Hattab, M., Hammad, T., and Fleureau, J.-M. 2015. "Internal friction angle variation in a
624 kaolin/montmorillonite clay mix and microstructural identification." *Géotechnique*,
625 65(1), 1–11. https://doi.org/10.1680/geot.13.P.081.

626 Hicher, P.-Y., Wahyudi, H., and Tessier, D. 2000. "Microstructural analysis of inherent and
627 induced anisotropy in clay." *Mech. Cohes.-Frict. Mater.*, 5(5), 341–
628 371.https://doi.org/10.1002/1099-1484(200007)5:5<341::AID-CFM99>3.0.CO;2-C.

629 Karstunen, M., and Yin, Z. Y. 2010. "Modelling time-dependent behaviour of Murro test
630 embankment." *Géotechnique*, 60(10), 735–749. https://doi.org/10.1680/geot.8.P.027.

631 Kong, L.W., Zhang, X. W., Guo, A. G., and Cai, Y. 2011. "Creep behavior of Zhanjiang
632 strong structured clay by drained triaxial test." [In Chinese] *Chine. J. Geotech. Eng.*,
633 30(2), 365-372.

634 Li, J. X., Wang, C. M., and Zhang, X. W. 2010. "Soft soil creep characteristics under different
635 drainage conditions and micropore changes." [In Chinese] *Rock Soil Mech.*, 31(11),
636 3493–3498.

637 Mesri, G., and Goldewski, P. M. 1977. "Time and stress-compressibility interrelationship." *J.*
638 *Geotech. Engng.*, 103: 5, 417–430. https://doi.org/10.1016/0148-9062(77)91005-1.

639 Mesri, G., and Choi, Y. K. 1985. "Settlement analysis of embankments on soft clays." *J.*
640 *Geotech. Eng.*, 441–465. https://doi.org/10.1061/(ASCE)0733-9410(1985)111:4(441).

641 Mitchell, J. K., and Soga, K. 2005. Fundamentals of soil behaviour. 3rd Ed., John Wiley&
642 Sons, Hoboken, New Jersey.

643 O'Reilly, M. P., Mair, R. J., and Alderman, G. H. 1991. "Long-term settlements over tunnels:
644 an eleven-year study at Grimsby." *Proc. Tunnelling '91, London, 6th International*
645 *Symposium*, 4, 55–64.https://doi.org/10.1016/0148-9062(92)92317-6.

Rothenburg, L., and Bathurst, R.J. 1989. “Analytical study of induced anisotropy in idealized granular-materials.” *Geotechnique*, 39 (4), 601–614. https://doi.org/10.1016/0148-9062(90)94374-3.

Rowe, R., and Hinchberger, S. D. 1998. “The significance of rate effects in modelling the Sackville test embankment.” *Can. Geotech. J.*, 35, 500–516. https://doi.org/10.1139/t98-021.

Singh, A., Mitchell, J. K. 1968. “General stress-strain-time function for soils.” *J. Soil Mech. Found. Div.*, 94(1):19–46.

Sekiguchi, H. 1973. “Flow characteristics of clays.” *Soils Found.*, 13(1), 45–60. https://doi.org/10.3208/sandf1972.13.45.

Sun, J. 2007. “Rock rheological mechanics and its advance in engineering applications.” [In Chinese] *Chin. J. Rock Mech. Eng.*, 26(6), 1081-1106.

Tavenas, F., Leroueil, S., Rochelle, P. L., and Roy, M. 1978. “Creep behaviour of an undisturbed lightly overconsolidated clay.” *Can. Geotech. J.*, 15(3), 402–423.https://doi.org/10.1139/t78-037.

Tavenas, F., and Leroueil, S. 1981. “Creep and failure of slopes in clays.” *Can. Geotech. J.*, 18(1), 106–120. https://doi.org/10.1139/t81-010.

Tian, W. M., Silva, A. J., Veyera, G. E., and Sadd, M. H. 1994. “Drained creep of undisturbed cohesive marine sediments.” *Can. Geotech. J.*, 31(6):841–855. https://doi.org/10.1139/t94-101.

Wang, P., and Yin, Z.-Y. 2020. “Micro-mechanical analysis of caisson foundation in sand using DEM.” *Ocean Engineering*, https://doi.org/10.1016/j.oceaneng.2020.107921.

Xie, X., Qi, S., Zhao, F., and Wang, D. 2018. “Creep behavior and the microstructural evolution of loess-like soil from Xi'an area, China.” *Engineering Geology*, 236: 43–59. https://doi.org/10.1016/j.enggeo.2017.11.003.

Yin, Z.-Y., Chang, C.S., Hicher, P. Y., and Karstunen, M. 2009. Micromechanical analysis of kinematic hardening in natural clay. *Int. J. Plast.*, 25(8): 1413-1435.

Yin, Z. Y., Xu, Q., and Yu, C. 2015. “Elastic viscoplastic modeling for natural soft clays considering nonlinear creep.” *Int. J. Geomech. ASCE*, 15(5): A6014001.https://doi.org/10.1061/(ASCE)GM.1943-5622.0000284.

Yin, Z. Y., Zhu, Q. Y., and Zhang, D. M. 2017. “Comparison of two creep degradation modeling approaches for soft structured soils.” *Acta Geotech.*, 12(6), 1395–1413.https://doi.org/10.1007/s11440-017-0556-y.

Yin, Z. Y., Zhao, J., and Hicher, P.Y. 2014. A micromechanics-based model for sand-silt mixtures. Int. J. *Solids Struct.*, 51(6): 1350-1363.

Yu, C., Wang, H., Zhou, A. N., Cai, X. Q., and Wu, Z. X. 2019. “Experimental study on strength and microstructure of cemented soil with different suctions.” J. Materials Civil Eng., 31(6): 04019082. https://doi.org/10.1061/(ASCE)MT.1943-5533.0002717.

Zhang, Z.L., and Cui, Z.D. 2017. “Analysis of microscopic pore structures of the silty clay before and after freezing–thawing under the subway vibration loading.” *Environ. Earth Sci.*, 76 (15), 528. https://doi.org/10.1007/s12665-017-6879-z.

Zhao, C.F., Yin, Z.Y., and Hicher, P.Y. 2018. Integrating a micromechanical model for multiscale analyses. *Int. J. Numer. Methods Eng.*, 114(2): 105-127.

689 Zhao, D., Hattab, M., Yin, Z. Y., and Hicher, P.-Y. 2019. “Dilative behavior of kaolinite
690 under drained creep condition.” *Acta Geotech.*, 14(4), 1003–1019.
691 https://doi.org/10.1007/s11440-018-0686-x.

692 Zhao, D., Gao, Q. F., Hattab, M., Hicher, P.-Y., and Yin, Z. Y. 2020. “Microstructural
693 evolution of remolded clay related to creep.” *Transp. Geotech.*, 24,
694 100367.https://doi.org/10.1016/j.trgeo.2020.100367.

695 Zhu, J. G. 2007. Rheological behavior and elastic viscoplastic modeling of soil. Science Press,
696 Beijing, China.

697 Zhu, Q. Y., Wu, Z. X., Li, Y. L., Wang, J. H., and Xia, X. H. 2014. “A modified creep index
698 and its application to viscoplastic modelling of soft clays.” *J. Zhejiang Univ.-SC. A*,
699 14(4), 272-281.https://doi.org/10.1631/jzus.A1300331.

700 # Table

701 **Table 1** Triaxial tests on Kaolin K13 clay

Test No.	p'_{010} (kPa)	p'_i (kPa)	q (kPa)	OCR	SL	η(=q/ p'_i)
$(P_{010}\text{-NC-q670})_{shear}$	1000	1000	670	1	0.78	0.67
$(P_{010}\text{-NC-q200})_{shear}$		1000	200	1	0.23	0.2
$(P_{010}\text{-OCR1.5-q445})_{shear}$		666	445	1.5	0.78	0.67
$(P_{010}\text{-OCR1.5-q200})_{shear}$		666	200	1.5	0.35	0.3
$(P_{010}\text{-OCR4-q200})_{shear}$		250	200	4	0.93	0.8
$(P_{010}\text{-NC-q670})_{creep}$	1000	1000	670	1	0.78	0.67
$(P_{010}\text{-NC-q200})_{creep}$		1000	200	1	0.23	0.2
$(P_{010}\text{-OCR1.5-q445})_{creep}$		666	445	1.5	0.78	0.67
$(P_{010}\text{-OCR1.5-q200})_{creep}$		666	200	1.5	0.35	0.3
$(P_{010}\text{-OCR4-q200})_{creep}$		250	200	4	0.93	0.8

702

Figure captions

Fig. 1 Loading state of triaxial tests in (p' -q) plane

Fig. 2 Image processing method: (a) SEM image; (b) particle representation; (c) orientation curve; (d) binary image; (e) ellipses fitting; (f) schematic plot of the pore geometry

Fig. 3 Strain versus stress along monotonic loading for NC tests

Fig. 4 Evolution of creep deformation for NC tests: (a) creep strain (b) creep strain rate

Fig. 5 Microfabric of tests P_{010}-NC-q670 in contractancy domain: (a) after shear (b) after creep

Fig. 6 Strain versus stress along monotonic loading for tests OCR=1.5

Fig. 7 Evolution of creep deformation for tests OCR=1.5: (a) creep strain (b) creep strain rate

Fig. 8 SEM images of tests OCR1.5 after shear: (a) in pseudo-elastic domain (b) in contractancy domain

Fig. 9 SEM images of tests OCR1.5 after creep: (a) in pseudo-elastic domain (b) in contractancy domain

Fig. 10 Global particle orientation of specimens in NC tests: (a) after shear (b) q=200 kPa (c) q=670 kPa (d) after creep

Fig. 11 Global particle orientation of specimens in OCR=1.5 test: (a) after shear (b) q=200 kPa (c) q=445 kPa (d) after creep

Fig. 12 Pore orientation versus stress level of NC tests: (a) after shear (b) after creep

Fig. 13 Evolution of pore shape for NC tests after shear: (a) roundness (b) length (c) diameter

Fig. 14 Evolution of pore shape for NC tests after creep: (a) roundness (b) length (c) diameter

Fig. 15 Pore orientation versus stress level of tests OCR=1.5: (a) after shear (b) after creep

Fig. 16 Evolution of pore shape for tests OCR=1.5: (a) roundness (b) length (c) diameter

Fig. 17 Evolution of creep deformation for tests under stress level at η = 0.67: (a) creep strain (b) creep strain rate

Fig. 18 Global particle orientation of specimens under final stress level at η = 0.67: (a) after shear (b) after creep

Fig. 19 Global pore orientation of specimens under final stress level at η= 0.67: (a) after shear (b) after creep

Fig. 20 Evolution of pore shapes for creep samples under stress level at η= 0.67: (a) roundness (b) length (c) diameter

Fig. 21 Evolution of microstructure with *SL* of NC samples: (a) isotropic index (b) pore shape

Fig. 22 Illustration of microstructure evolution in different volumetric domains

Fig. 23 Evolution of microstructure with *SL* of samples OCR=1.5: (a) isotropic index (b) pore shape

Fig. 24 Local coordinate at inter-particle contact

Fig. 25 Fabric evolution of particles

Figure 1

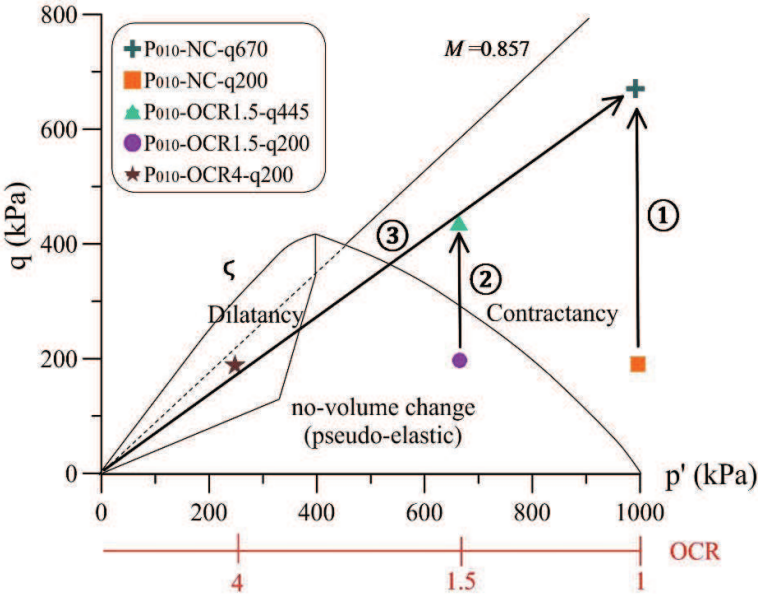

Figure 2

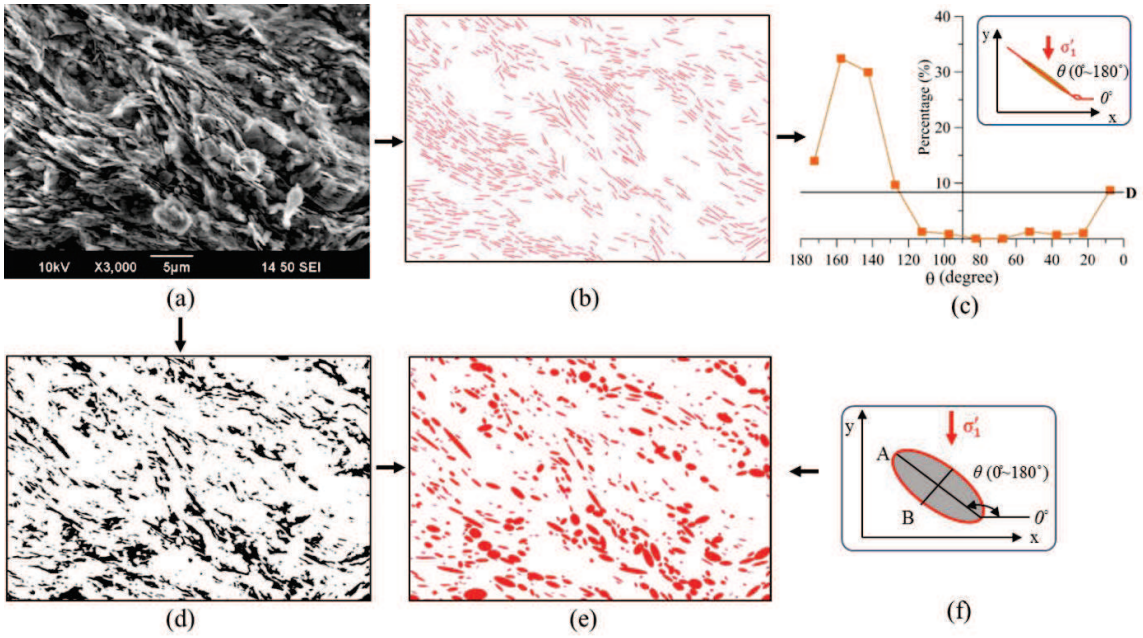

Figure 3

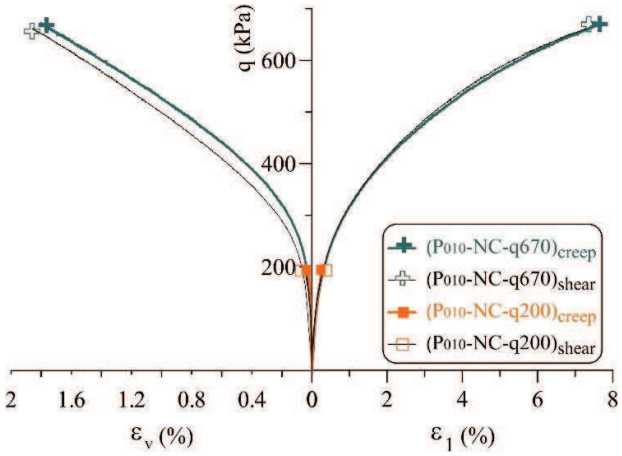

Figure 4

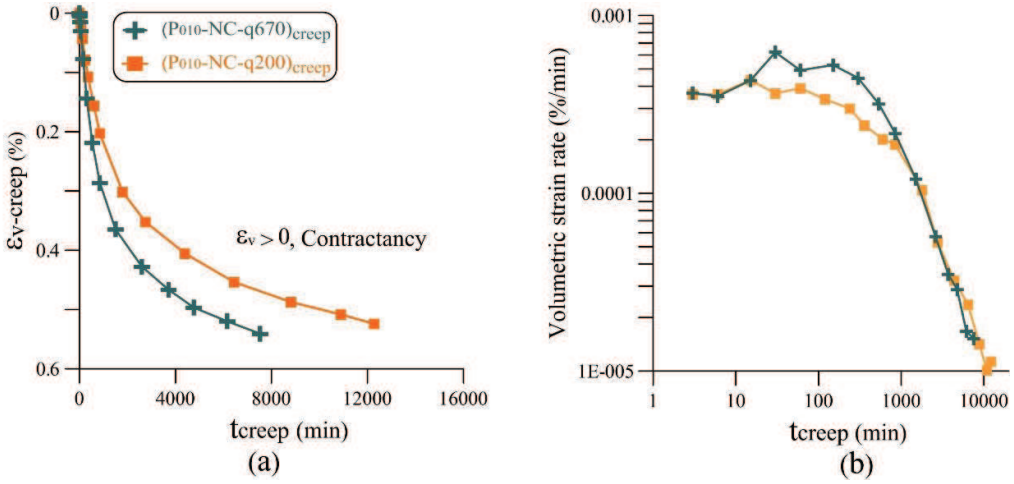

Figure 5

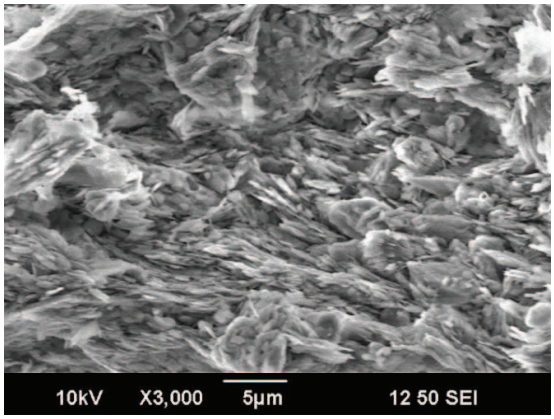

(a)

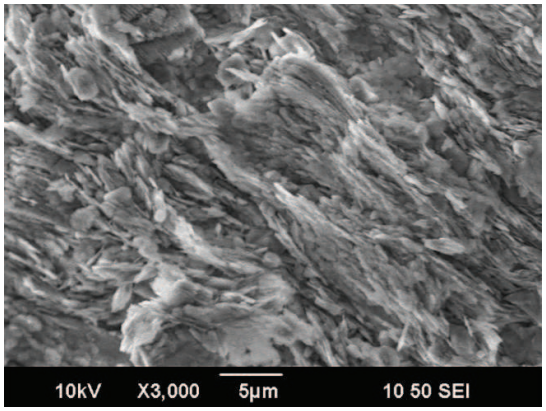

(b)

Figure 6

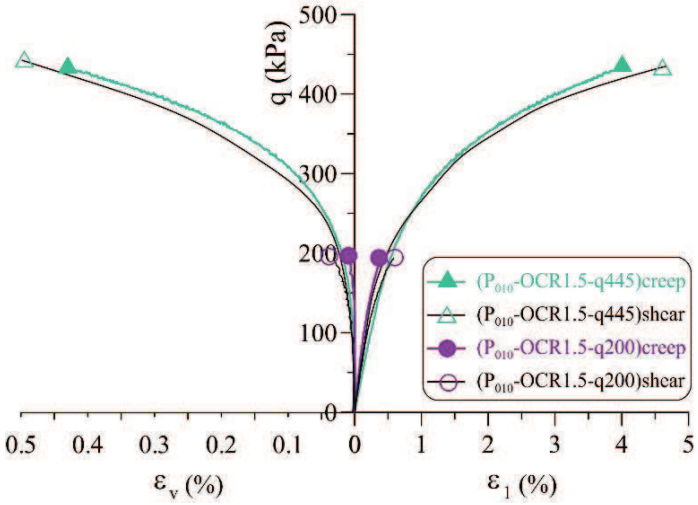

Figure 7

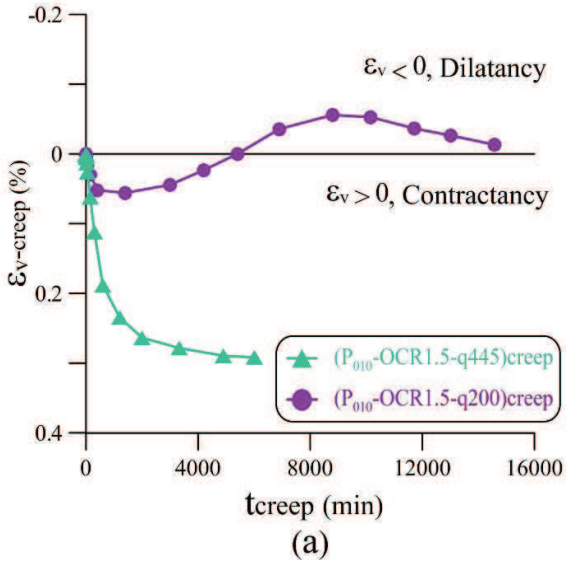

(a)

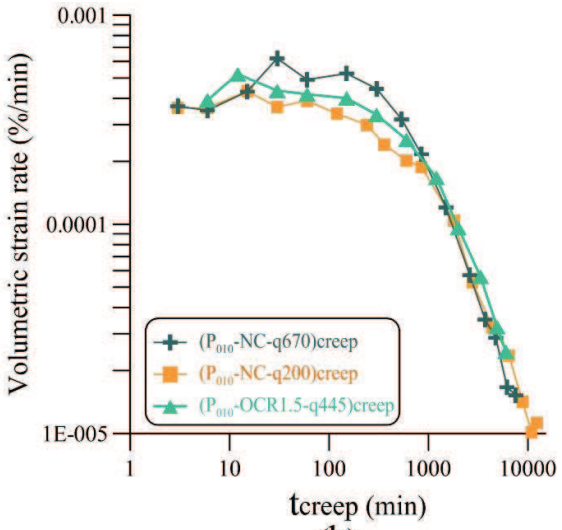

(b)

Figure 8

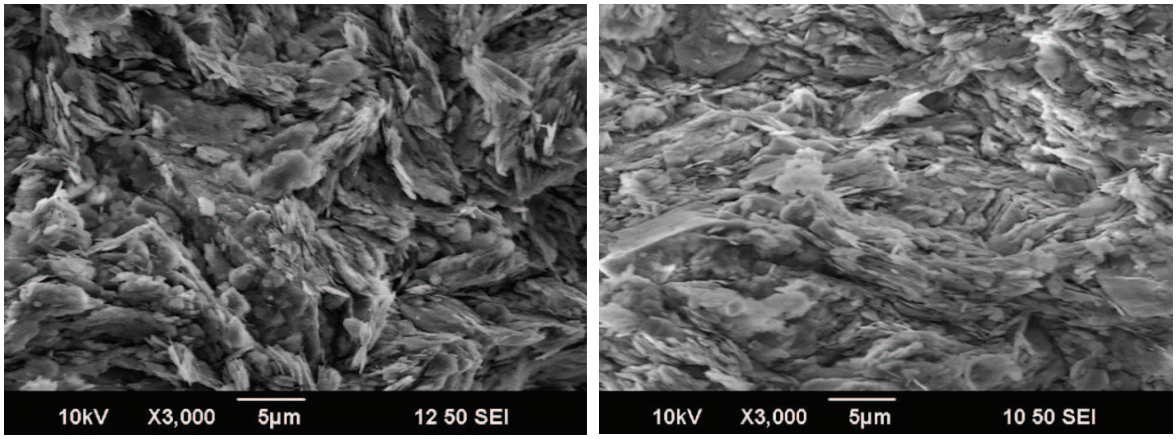

(a) (b)

Figure 9

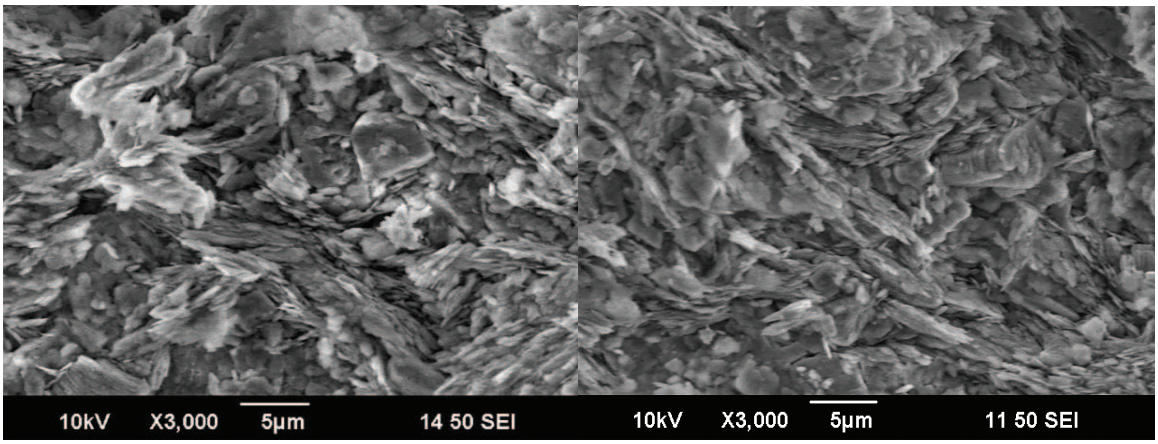

(a) (b)

Figure 10

Click here to access/download;Figure;Figure_10.eps

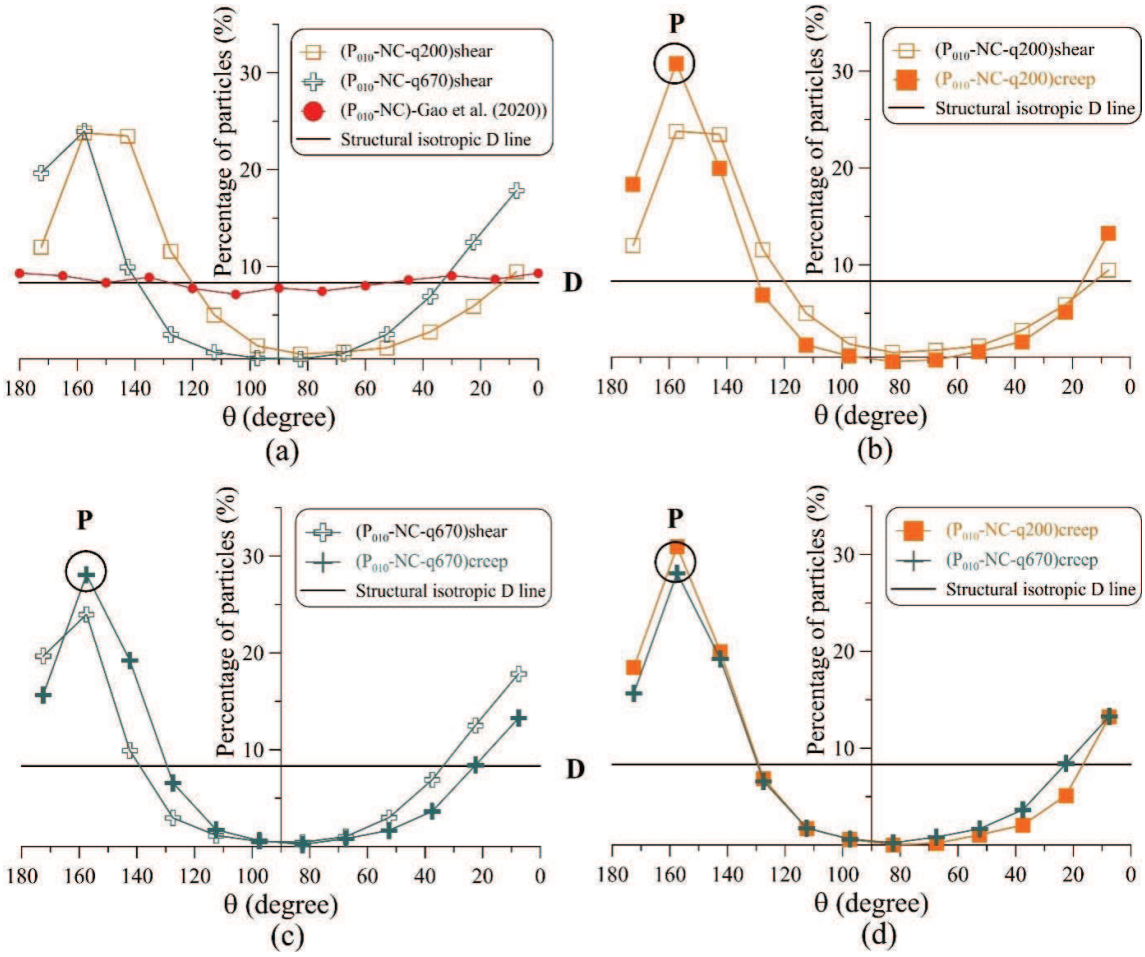

Figure 11

Click here to access/download;Figure;Figure_11.eps

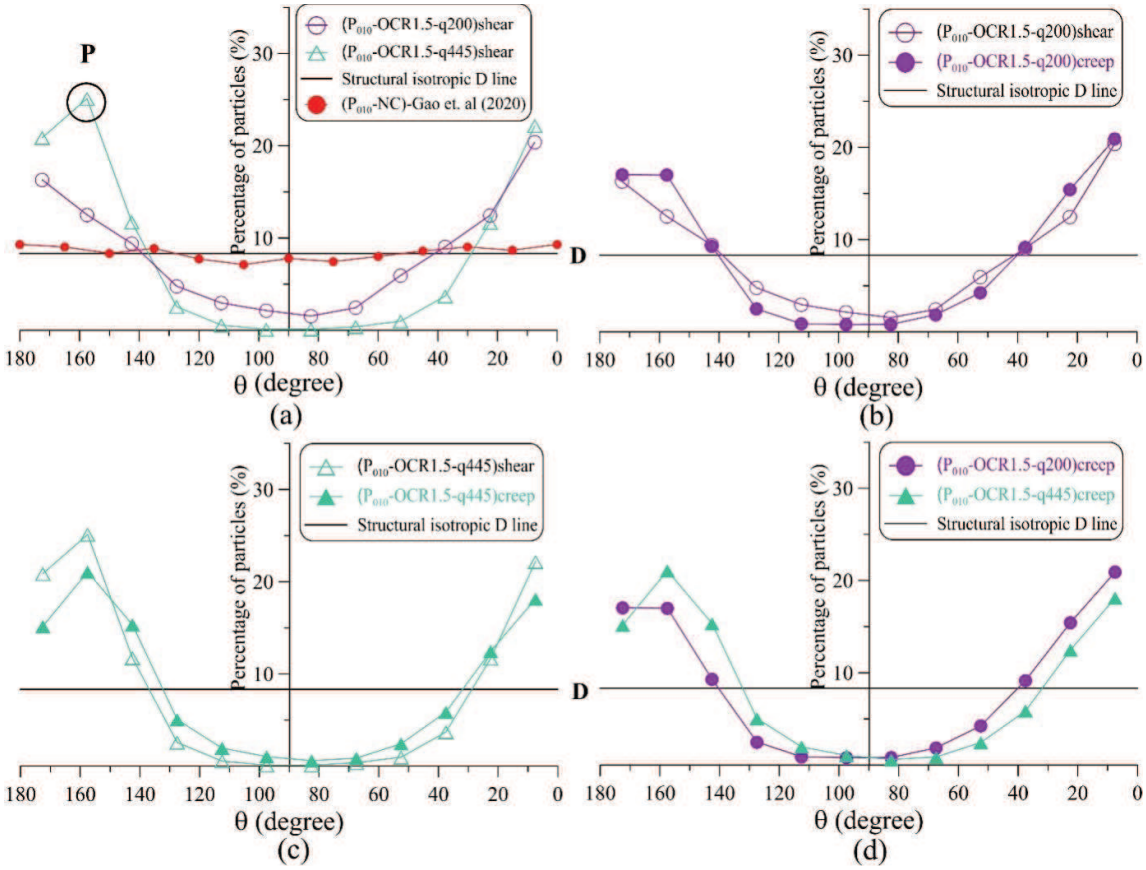

Figure 12

Click here to access/download;Figure;Figure_12.eps

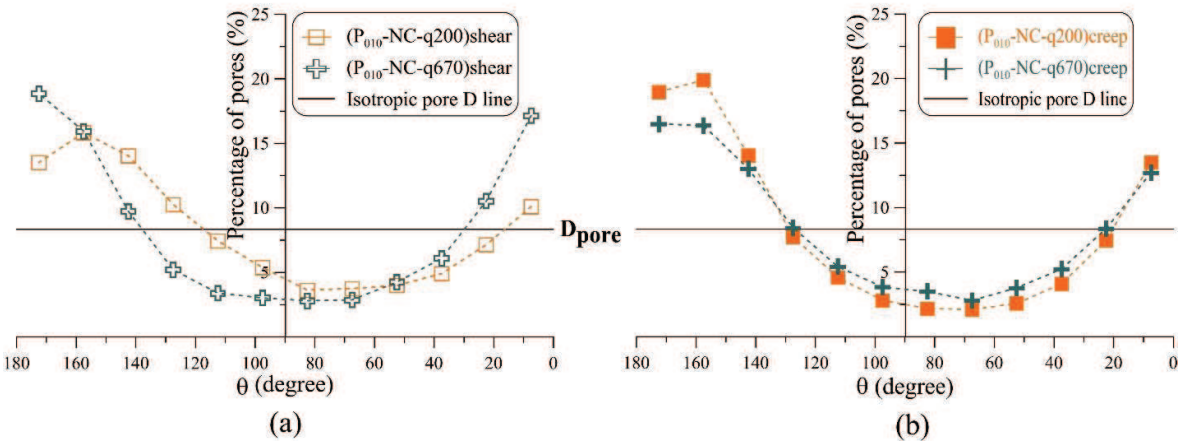

Figure 13

Click here to access/download;Figure;Figure_13.eps

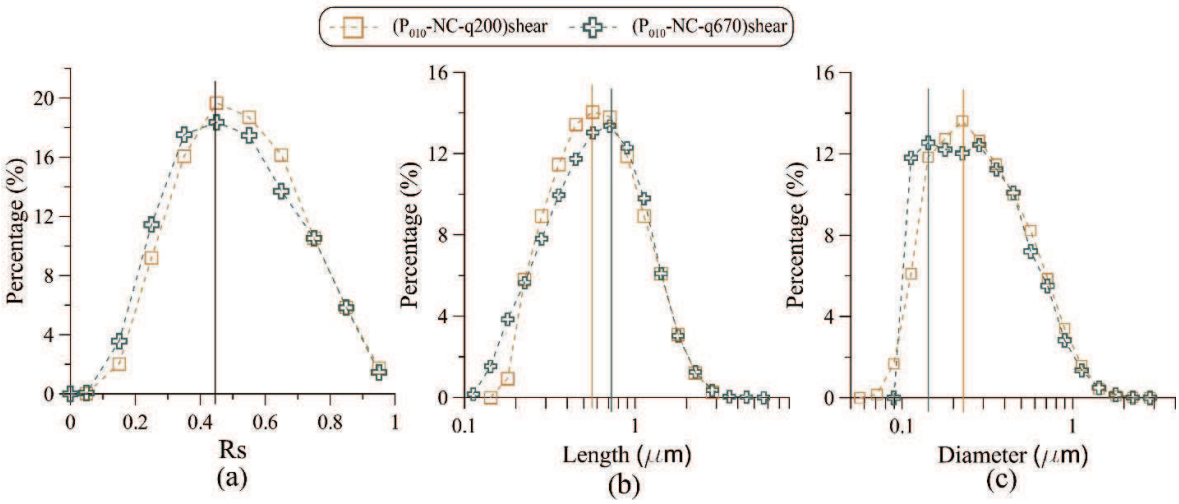

Figure 14

Click here to access/download;Figure;Figure_14.eps

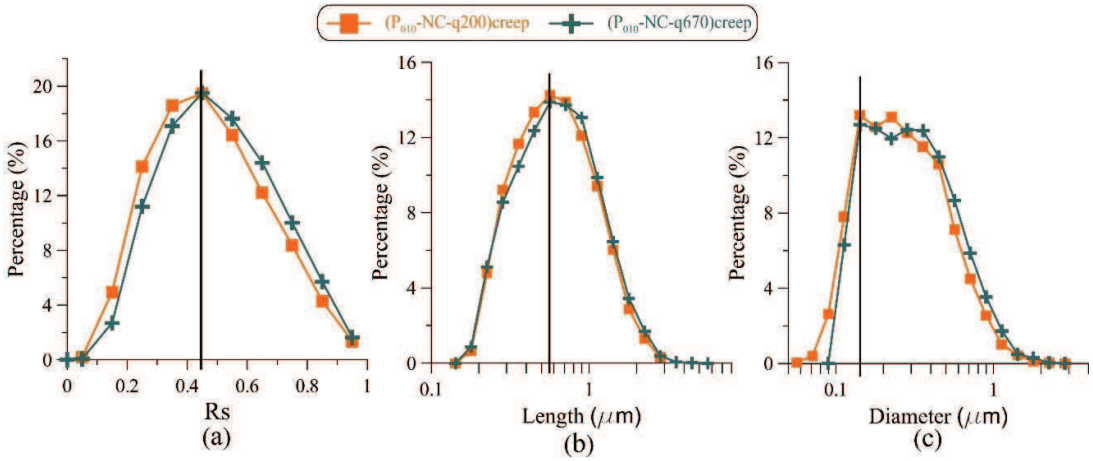

Figure 15

Click here to access/download;Figure;Figure_15.eps

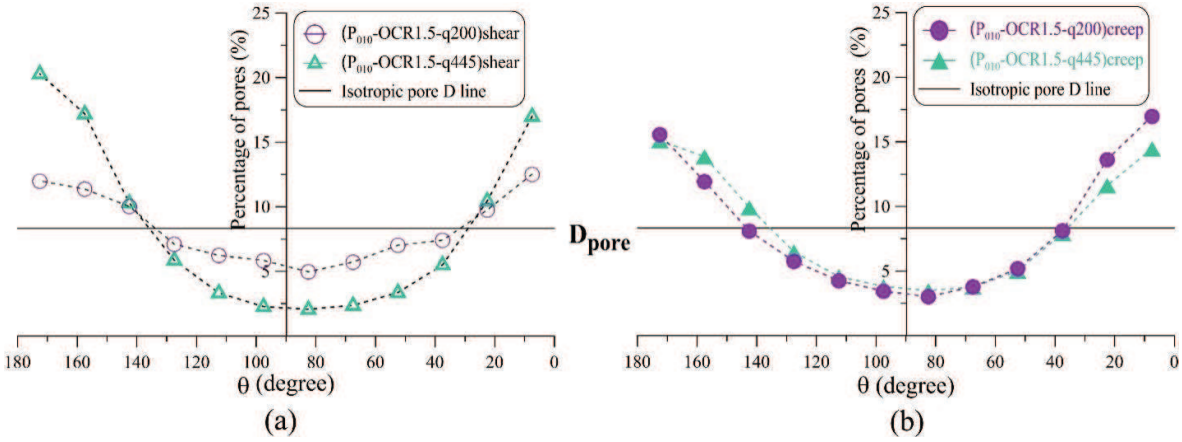

Figure 16

Click here to access/download;Figure;Figure_16.eps

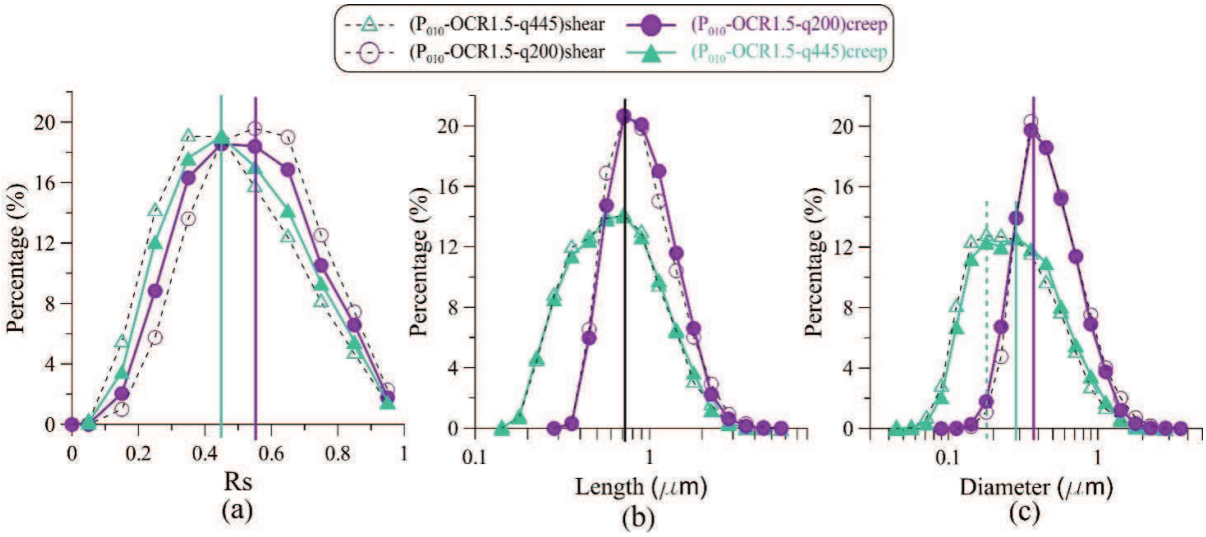

Figure 17

Click here to access/download;Figure;Figure_17.eps

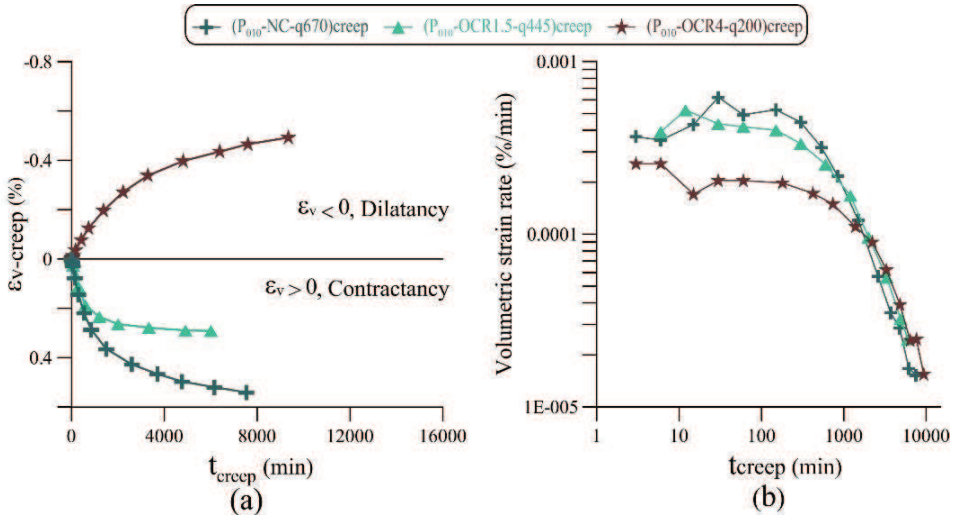

Figure 18

Click here to access/download;Figure;Figure_18.eps

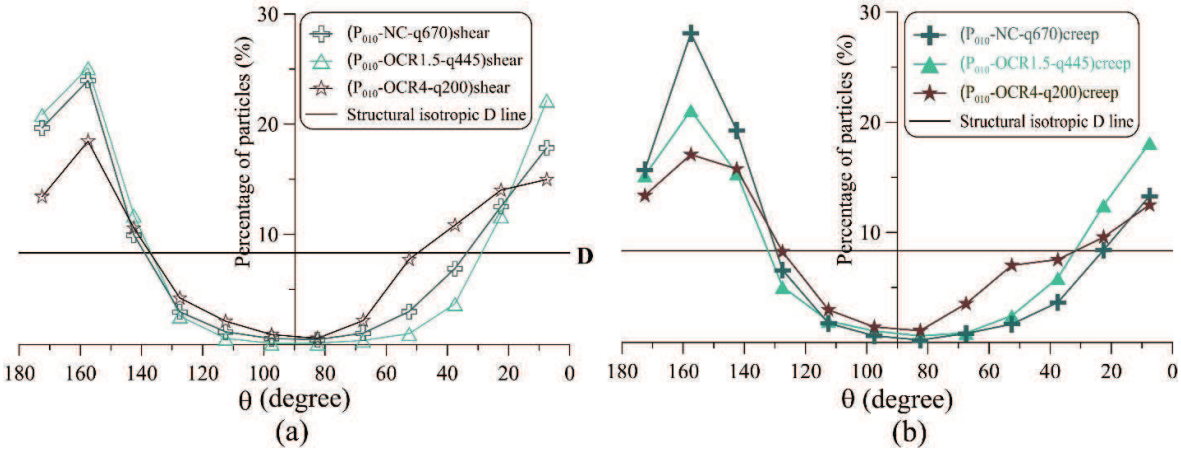

Figure 19

Click here to access/download;Figure;Figure_19.eps

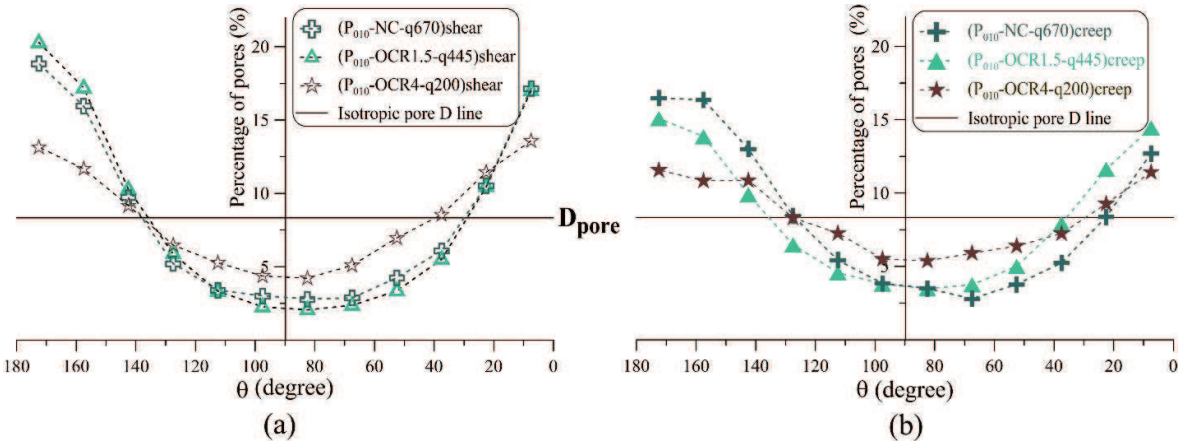

Figure 20

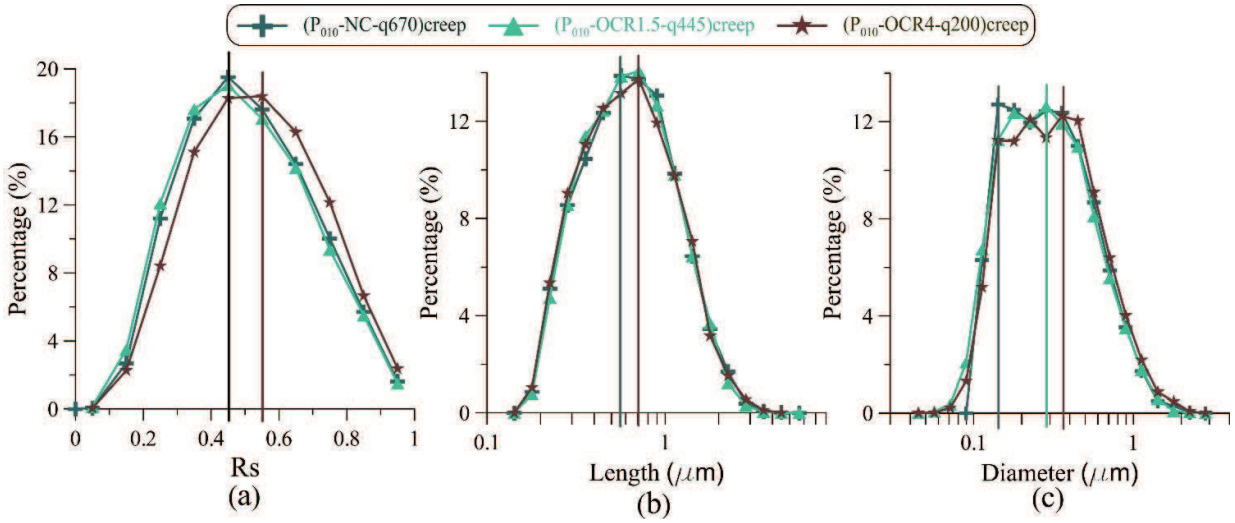

Figure 21

Click here to access/download;Figure;Figure_21.eps

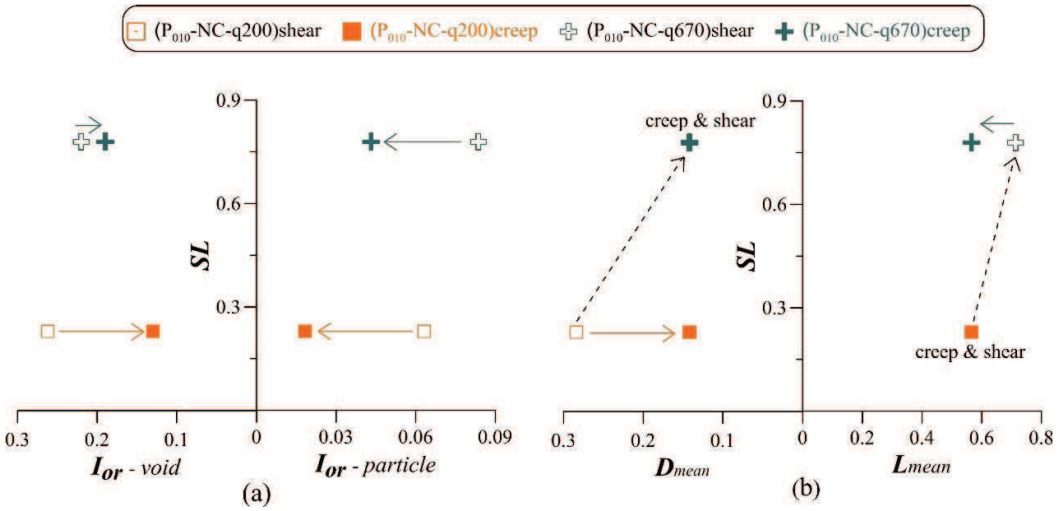

Figure 22

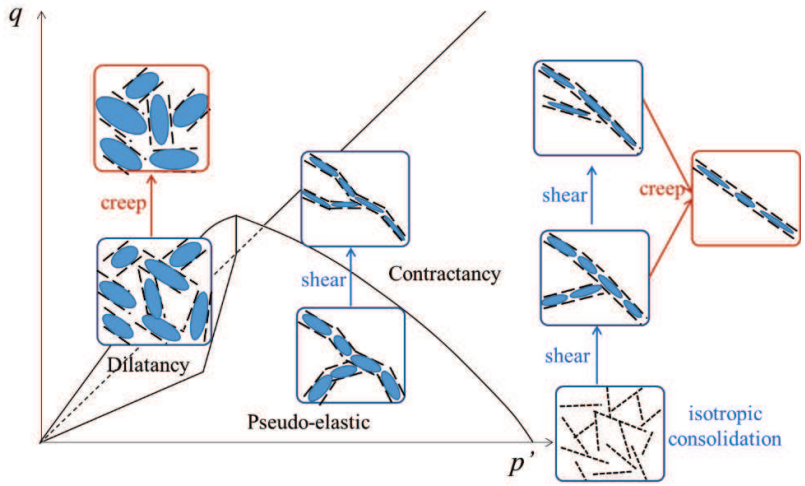

Figure 23

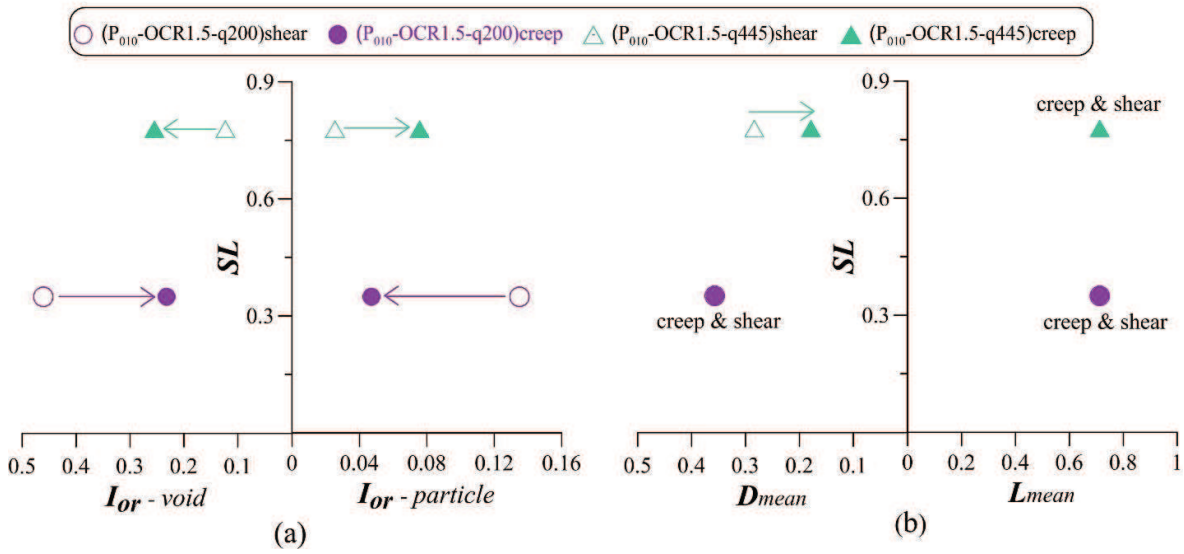

Figure 24

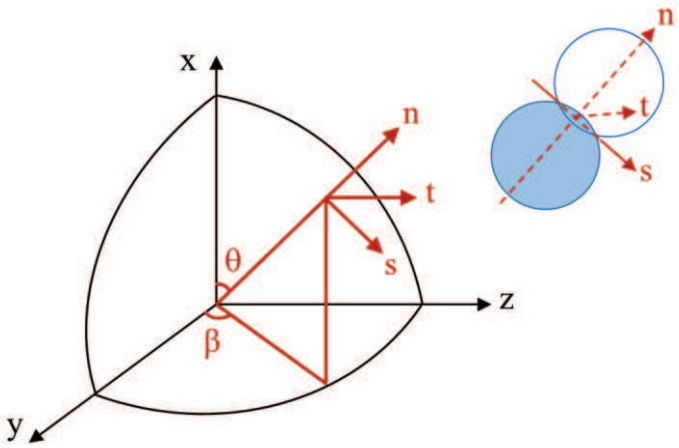

Test No.	Shear test	Creep test
P_{010}-NC	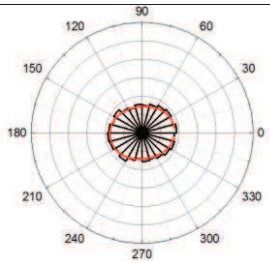 a = 0.11, θ_a= 7.5˚	
P_{010}-NC-q670	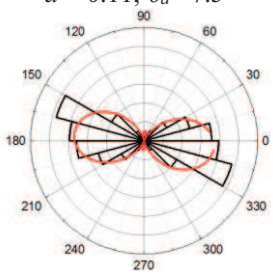 a = 1.33, θ_a= -5˚	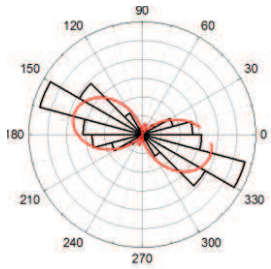 a = 1.37, θ_a= -16˚
P_{010}-NC-q200	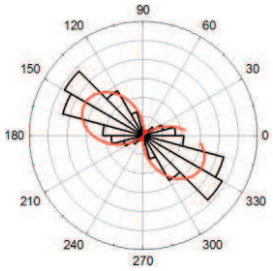 a = 1.20, θ_a= -28˚	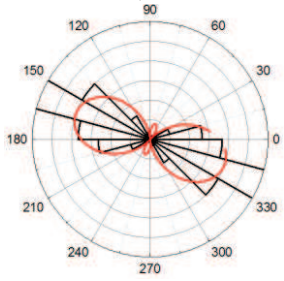 a = 1.51, θ_a= -19˚
P_{010}-OCR1.5-q200	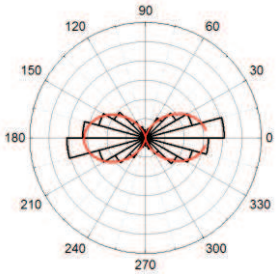 a = 1.00, θ_a= 0˚	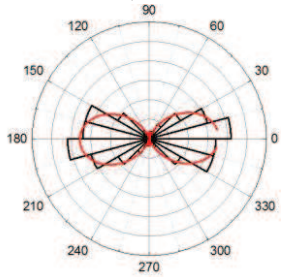 a = 1.24, θ_a= 1˚
P_{010}-OCR4-q200	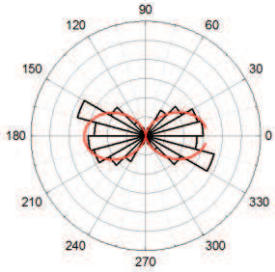 a = 1.01, θ_a= 0.5˚	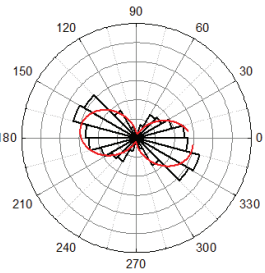 a = 0.87, θ_a= -10˚